Journal of MATERIALS RESEARCH

Article
DOI:10.1557/s43578-023-00945-7

Nanocrystal composite ($CoFe_2O_4$)/(Mg) for photocatalyst of methylene blue and Congo red: stability structural properties from X-ray diffraction and chemical bonding from infra-red spectroscopy

Nurul Fauziah[1], Syarifuddin Syarifuddin[1], Heryanto Heryanto[1], Dahlang Tahir[1,a)]

[1] Department of Physics, Hasanuddin University, Makassar 90245, Indonesia
[a)] Address all correspondence to this author. e-mail: dtahir@fmipa.unhas.ac.id

Received: 4 October 2022; accepted: 9 February 2023; published online: 6 March 2023

The ability of $CoFe_2O_4$/Mg composite to degrade pollutants and be used repeatedly indicates that it has a high potential as a new candidate material for reducing the environmental pollution. This study aims to investigate the effect of Mg in $CoFe_2O_4$/Mg composite on the performance of photocatalysts for textile wastewater treatment. The sol–gel method was used to synthesize $CoFe_2O_4$/Mg powder, which was then characterized using Fourier transform infrared (FTIR), X-ray diffraction (XRD), and UV–visible (UV–vis) spectroscopy. The average crystal size and splitting between two optical phonon modes decrease with increasing Mg concentration in the composite. Composite band gaps are 2.48 eV, 2.72 eV, and 2.94 eV for 0% Mg, 30% Mg, and 50% Mg, respectively. The best degradation efficiency with a high kinetic rate constant of the photocatalyst is when the Mg concentration in the composite was 50%. The photocatalyst degradation efficiency is due to Mg-mediated electron and hole recombination rate suppression. The XRD and FTIR spectra for 50% Mg before and after textile wastewater degradation show structural stability, confirmed by five degradation cycles. The scanning electron microscope shows surface image olid surfaces with the agglomeration of $CoFe_2O_4$ and Mg atoms and a wide surface. This suggests that it could be a new composite.as a promising catalyst.

Introduction

As the human population grows, so does the demand for daily necessities, resulting in rapid industrial developments. Industrial growth has triggered environmental problems worldwide, including wastewater, one of the most encountered problems [1, 2]. The textile industry is the largest contributor to wastewater; approximately 10,000 dyes and pigments are produced globally each year. Natural and synthetic dyes are used in the textile industry, and approximately 20–30% of them are wasted during processing [3]. Water pollution is harmful to the environment because toxic water contains fertilizers, chlorinated solvents, and dyes that are difficult to decompose [1, 3–5].Photodegradation in the advanced oxidation process (AOP) is one environmentally friendly way to reduce the impact of water pollution [6]. There are many ways to treat wastewater with AOP. Photocatalysis is preferred due to its environmental friendliness, low toxicity, low cost, and antibacterial activity [7]. Furthermore, it also makes good use of solar energy to degrade wastewater via oxidation–reduction reactions [8, 9].

One of the promising photocatalytic materials is metal oxides, which have varied bandgaps, enhancing their sunlight absorption capability over a wide range, reducing charge recombination, and are also inexpensive, such as spinel ferrite [10]. Among the various spinel ferrites, cobalt ferrite ($CoFe_2O_4$) stands out due to its high magnetization yield, low cost-effectiveness, form versatility, chemical and mechanical stability, and low toxicity [11–13]. $CoFe_2O_4$ was employed as a photocatalyst for degrading organic contaminants because it has a low bandgap of 1.76 eV [14]. However, pure $CoFe_2O_4$ has a high electron and hole recombination rate, thus affecting the performance of the photocatalyst. To improve the photocatalytic performance of $CoFe_2O_4$ composite-based photocatalysts, a co-catalyst made

of metal or polymer should be added via a Schottky junction, which is useful in forming charge spaces between two materials to aid in electron transport [15]. The electrons captured by the Schottky junction will be transferred from the semiconductor to the doped material, and the metal co-catalyst will prevent electrons from flowing back to the $CoFe_2O_4$, thereby suppressing the recombination of photogenerated electrons and holes [16, 17]. The performance of the photocatalyst $CoFe_2O_4$ with various composite materials based on several previous studies was reported [9, 18–20], wherein the composites could degrade dye pollutants up to 97.3%. Magnesium (Mg) is one such material that can be used as an alternative to improve the performance of $CoFe_2O_4$ composite-based photocatalysts. Mg has biodegradation and biocompatibility properties; when in the form of magnesium oxide, it has a wide band gap of about 7.8 eV [21].

Microwave, sol–gel, hydrothermal, thermal decomposition, and co-precipitation [22] are the methods used to synthesize cobalt ferrite materials. Because the composition, purity, homogeneity, particle size, and distribution of ferrite can be controlled, sol–gel synthesis is one of the most commonly used [23]. On the other hand, mechanical alloying is widely used for synthesized composites due to easily producing nanoscale alloys [24]. However, there are no reported references for the synthesis of $CoFe_2O_4$/Mg in two steps: the sol–gel method for CoFe2O4 and the simple mechanical alloying method. As a result, in this study, we used these two synthesized methods to create $CoFe_2O_4$/Mg composites with varying Mg concentrations, which we then used as photocatalysts material for degrading Congo red and methylene blue as textile waste models. X-ray diffraction (XRD), Fourier transform infrared (FTIR), and UV–visible (UV–vis) spectrophotometers were used to examine the photocatalyst material and degradation efficiency. In addition, the recyclability, XRD, and FTIR were used to analyze the stability of composite $CoFe_2O_4$/Mg in degrading Congo red and methylene blue.

Results and discussion

XRD

Figure 1(a) shows XRD spectra of $CoFe_2O_4$ (Mg 0%), 30% Mg, and 50% Mg and for (b) zoom in diffraction peak at 34° to 39° to identify shifts diffraction peaks with additional Mg. The 30% Mg photocatalyst shifted to the lowest 2θ indicating enlarging d-spacing whereas the 50% Mg shifted to the highest 2θ indicating reducing d-spacing, as shown in two and three dimensions in Fig. 1(c). The two and three dimensions show how the atoms bonding together with oxide or bonding between $CoFe_2O_4$ and Mg atoms. The diffraction peaks of $CoFe_2O_4$ show diffraction peaks formed at 2θ: 18.14°, 30.13°, 35.48°, 37.09°, 43.09°, 53.56°, and 57.03° corresponding with crystal plane (hkl) is (111), (220), (311), (222), (400), (422), and (511), respectively. These results have been confirmed by the standard XRD pattern (space group Fd-3 m, JCPDS: 00–022-1086) [3, 9, 12]. The diffraction peaks of Mg at 2θ: 32.48°, 34.69°, 36.91° (MgO), 48.12°, and 57.36° for crystal plane: (100), (002), (101), (102), and (110), respectively [25, 26]. The formation of the Fe_3O_4 phase shows at 2θ 33.61 (JCPDS: 00-003-0863).

The crystal orientations (110) of Mg and (511) of $CoFe_2O_4$ overlap, resulting in the formation of the composite $CoFe_2O_4$/Mg, indicating Mg has been successfully attached to the $CoFe_2O_4$ lattice [9]. Figure 1(b) also shows the diffraction peak intensities of $CoFe_2O_4$ decreased and experienced a shift in the diffraction peaks after adding Mg to the composite. The peak with the crystal orientation (311), which shifts to a lower angle, indicates Mg incorporation into the $CoFe_2O_4$ lattice [27]. The peak shifted to a higher angle at higher Mg concentrations due to substituting Mg^{2+} ions in cobalt ferrite particles [28].

Debye Scherrer is used for calculating the average crystallite size, which is as follows [8]:

$$D = \frac{K\lambda}{\beta \cos\theta} \quad (1)$$

where D denotes the crystallite size, K denotes the Scherrer constant is 0.9, β denotes the full width at half maximum and λ denotes the X-ray wavelength for the Cu source, which is 1.5406. The average crystallite size for $CoFe_2O_4$ (Mg 0%), 30% Mg, and 50% Mg is 23.19 nm, 34.28 nm, and 27.08 nm, respectively. It appears that the average crystallite size for composite $CoFe_2O_4$/Mg decreases with increasing amount of Mg.

FTIR

Figure 2 shows FTIR spectra recorded in the wavenumber range 4000–350 cm^{-1}, at wavenumber (ν_1) in the range 580–588 cm^{-1} was assigned metal–oxygen (M–O) vibrations at the tetrahedral site (M is Co, Mg, and Fe), and at wavenumber (ν_2) in the range 386–389 cm^{-1} correspond to the vibrational strain of metal–oxygen bonds at the octahedral site [10, 29]. The peak shift of the ν_1 and ν_2 absorption bands to higher wave numbers is proportional to the increase in Mg concentration [29, 30]. Wavenumbers 3442–3446 cm^{-1} and 1641–1647 cm^{-1} are associated with the stretching vibrations of O–H [10, 30]. The wavenumbers 1385 to 1485 cm^{-1} correspond to the H–O–H bond mode, while the wavenumbers 2357 to 2926 cm^{-1} correspond to the stretching vibrations of C–O [31]. Utilizing the Krames–Kronig (K–K) relation, quantitative analysis of FTIR spectra is used to determine optical properties, dielectric functions, and energy loss functions. This method is described in detail in our previously published papers. [31–36] The methods for determining optical properties in the form of refractive index (n) and extinction coefficient (k) are briefly repeated below [37]. With the Lambert

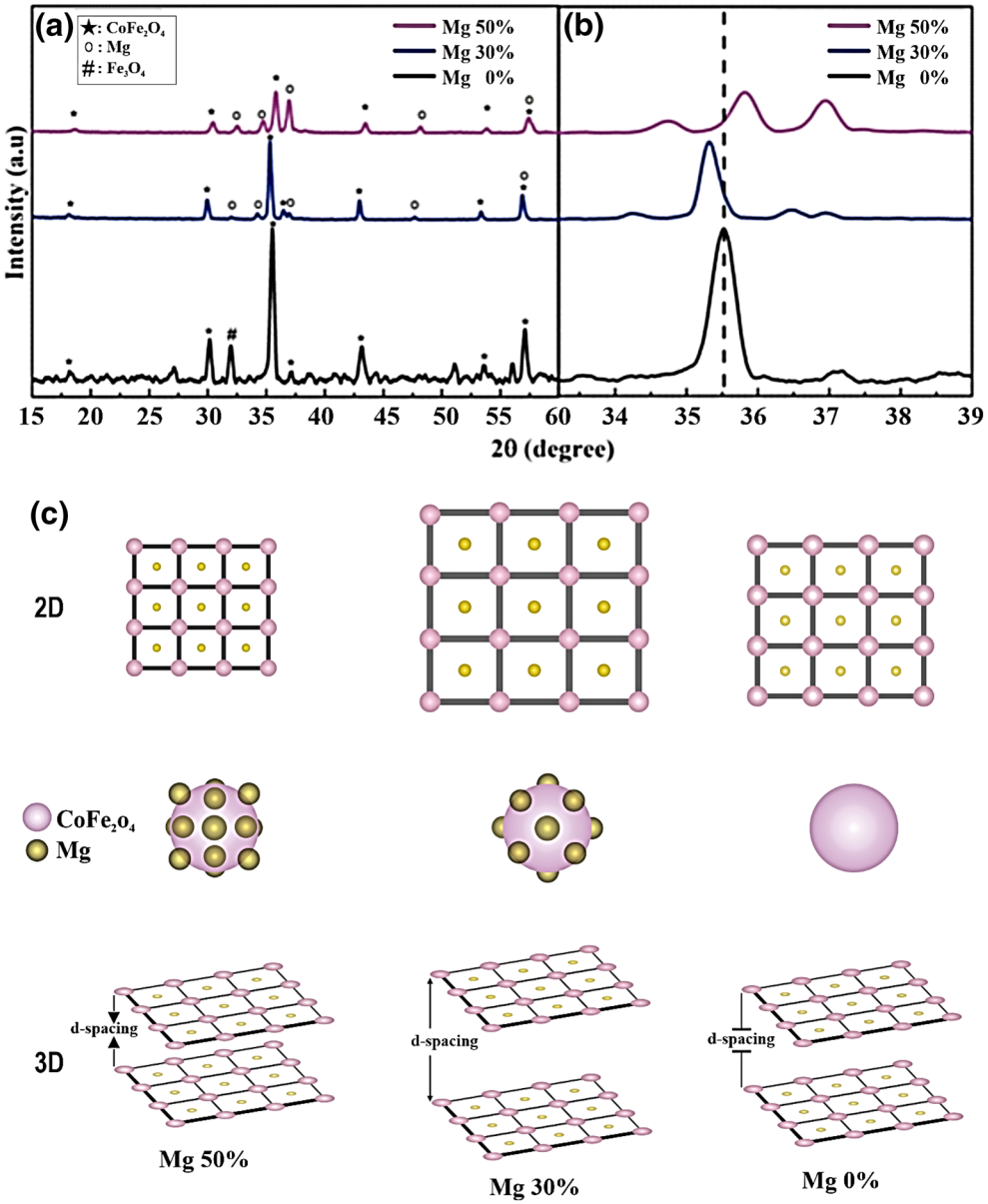

Figure 1: (a) XRD spectra for $CoFe_2O_4$ (Mg 0%), Mg 50%, and 30% in the form of composite $CoFe_2O_4$/Mg and (b) zoom of diffraction peaks for 34° to 39° and for crystal structures when the Mg atoms attached to the surface of $CoFe_2O_4$ and for 2 and 3 dimensional of the crystal structure when the spectra shifted to the left (lowest diffraction degree) or to the right (higher diffraction degree).

principle, the transmittance T (%) spectra will be converted to absorbance A (%) and then reflectance (R (%)) [37, 38]:

$$A(\omega) = \log \frac{I_0}{I} = \log \frac{1}{T(\omega)} = 2 - \log\left(T(\omega)\%\right) \quad (2)$$

$$R(\omega) = 100 - [T(\omega) + A(\omega)] \quad (3)$$

The refractive index in the complex form is [36]:

$$\tilde{n}(\omega) = n(\omega) + k(\omega) \quad (4)$$

where $n(\omega)$ denotes the real part and $k(\omega)$ denotes the imaginary part of the complex refractive index:

$$n(\omega) = \frac{1 - R(\omega)}{1 + R(\omega) - 2\sqrt{R(\omega)}\cos\phi(\omega)} \quad (5)$$

$$k(\omega) = \frac{2\sqrt{R(\omega)}\sin\phi(\omega)}{1 + R(\omega) - 2\sqrt{R(w)}\cos\phi(\omega)} \quad (6)$$

$\phi(\omega)$ is the phase change calculated from the dispersion of the K–K relation:

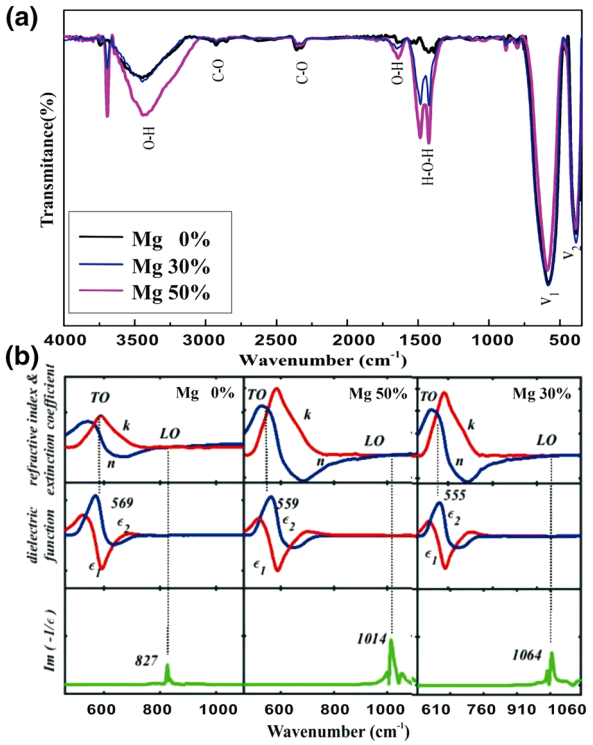

Figure 2: FTIR spectra $CoFe_2O_4$ (Mg 0%), 30% Mg, and 50% Mg (a) and the refractive index (n), extinction coefficient (k), dielectric function, and energy loss function (Im (-1 / ε)) (b).

TABLE 1: Transverse optical (TO), mode optical longitudinal (LO) mode of phonon vibration and Δ (LO – TO).

Material	TO	LO	Δ(LO – TO)
50% Mg	569	827	258
30% Mg	559	1014	455
$CoFe_2O_4$ (0% Mg)	555	1064	509

$$\phi(\omega) = \frac{-\omega}{\pi} \int_0^\infty \frac{\ln R(\omega') - \ln R(\omega)}{\omega'^2 - \omega^2} d\omega \tag{7}$$

by the Maclaurin method, the phase change becomes:

$$\phi(\omega_j) = \frac{4\omega_j}{\pi} . \Delta\omega . \sum_i \frac{\ln\left(\sqrt{R(\omega)}\right)}{\omega_i^2 - \omega_j^2} \tag{8}$$

where $\Delta\omega = \omega_{i+1} \pm \omega_i$. When the wave number j is odd, then, $i = 2,4,6,8, \ldots, j-1, j+1$, and if the wave number j is even number then $i = 1,3,5,7, \ldots, j-1, j+1$.

The optical properties in the form of n and k of $CoFe_2O_4$ (Mg 0%), 30% Mg, and 50% Mg are depicted in Fig. 2 (b), along with the corresponding values of transversal optical phonon mode (TO) and LO for longitudinal in Table 1. The TO increases with increasing Mg from 30% Mg to 50% Mg, whereas the LO increases conversely. The distance between the two optical phonon vibration modes (Δ (LO–TO)) is shown in Table 1. As the concentration of Mg increases, the Δ(LO–TO) decreases, indicating that small metal–oxygen (M–O) vibrations affect the large vibration of H–O–H and C–O bonds or vice versa. Conversely, higher Δ (LO–TO) indicates that the covalent bonds in the material are stable and strong [39].

As shown in Fig. 2, the imaginary part dielectric function (ε_2) can be used to confirm the TO wavenumber position (b). Determining the dielectric function of the real part (ε_1) and the imaginary part (ε_2) [34]:

$$\varepsilon_1(\omega) = n^2(\omega) - k^2(\omega) \tag{9}$$

$$\varepsilon_2(\omega) = 2n(\omega)k(\omega) \tag{10}$$

The LO phonon vibration mode can be confirmed from the peak position of the energy loss function (Im (− 1/ε$_1$ (ω)) according to Fig. 2(b) from [34]:

$$\mathrm{Im}\left(-\frac{1}{\varepsilon_1(\omega)}\right) = \frac{(\varepsilon_1(\omega))}{\left(\varepsilon_1^2(\omega) + \varepsilon_2^2(\omega)\right)} \tag{11}$$

Figure 2(b) demonstrates that the intensity of the Im (− 1/1) increases and becomes more distinct with increasing Mg in the composite, indicating that Mg was successfully incorporated into the atomic structure of $CoFe_2O_4$. [34, 40].

Band gap

The band gap was computed using the Kubelka–Munk equation [28, 41]:

$$\alpha h\nu = A\left(h\nu - E_g\right)^{1/2} \tag{12}$$

where E_g denotes the energy band gap, h denotes the plank constant, ν denotes the frequency of light, A denotes the proportional constant, and α denotes the absorption coefficient.

Figure 3(a) depicts the cutting results of the UV–vis absorption spectrum using Tauc's plot method to determine the bandgap, as indicated by the intersection line at $(\alpha h\nu)^2 = 0$. $CoFe_2O_4$ (Mg 0%), 30% Mg, and 50% Mg had respective bandgap values of 2.48 eV, 2.72 eV, and 2.94 eV. Due to the oxygen content in Fe_3O_4 binding with some of the Mg to form MgO, where MgO has a higher energy gap, the bandgap increases with increasing Mg concentration in the composite [21].

Photocatalyst analysis of composites for degradation of textile dyes

Photocatalyst activity

Using CR and MB as model wastewater pollutants, the photocatalytic activity of composites containing 30% and 50% Mg was examined. Figure 3(b) depicts the UV–vis absorption spectra

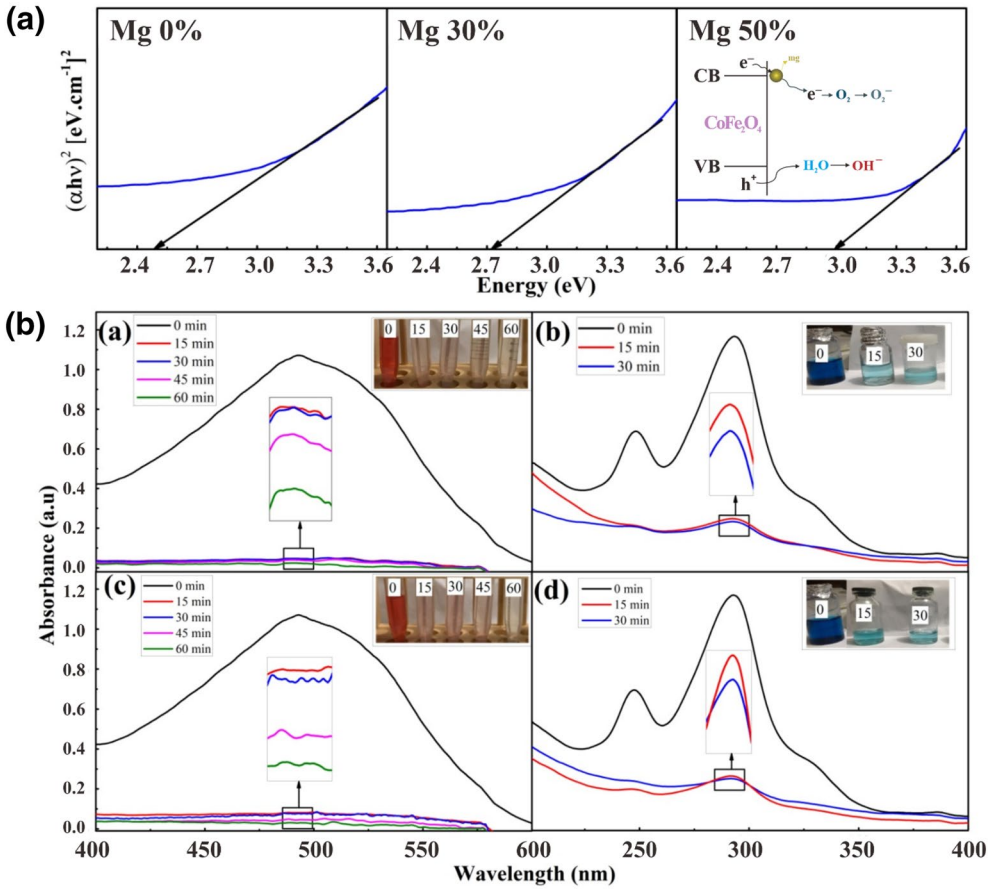

Figure 3: (a) The band gap of $CoFe_2O_4$ (Mg 0%), 30% Mg, and 50% Mg (a) and UV–vis spectra of composite with 30% Mg and 50% Mg used congo red (CR) and methylene blue (MB) as a pollutant model. The band diagrams of $CoFe_2O_4$/Mg are attached (closed) to the conduction band (CB) to help transport electrons through the surface for reaction with O_2 molecules. (b) Uv–vis spectra of $CoFe_2O_4$ for various irradiation time of CR for 30% Mg (1) and 50% Mg (3) and MB for 30% Mg (2) and 50% Mg (4).

of dyes CR and MB irradiated for 15 min with visible light. CR has an absorbance value of 400–600 nm, while MB has an absorbance value of 200–400 nm. It can be observed that as the irradiation time increases, the absorbance of both CR and MB decreases. Maximum absorbance was observed for CR at 493 nm and MB at 290 nm.

Figure 4 and Table 2 depict the degradation of composite 30% Mg and 50% Mg for CR and MB dyes, respectively. The percentage of degradation calculated by [42]:

$$\%\text{Degradation} = \frac{C_o - C}{C_o} \times 100 \tag{13}$$

where C denotes the final concentration and C_0 denotes the initial concentration. CR exhibits greater photocatalytic degradation than MB, likely because CR is an anionic dye and MB is a cationic dye. When interacting with anionic dyes, the photocatalyst material for the less oxygenated group causes electrostatic attraction. The impact of electrostatic attraction is the enhancement of the photocatalyst material's adsorption capacity by [43]. CR degrades in 60 min, whereas MB degrades in 30 min. The composite containing 50% Mg exhibits greater photodegradation because increasing Mg concentration increases the active site on the photocatalyst's surface, which plays a role in the photodegradation process [34]. This is also related to the fact that the average crystallite size of composite 50% Mg is smaller than that of 30% Mg, making it easier for charge carriers to participate in the photocatalytic process. For large crystallite size, the recombination of electrons and holes outside the barrier region will increase [40].

Kinetic rate constants of CR and MB were calculated using the pseudo-first-order reaction [35]:

$$\text{Ln}\frac{C_o}{C_t} = k.t \tag{14}$$

where C_0 denotes the initial concentration of the dye, C_t denotes the dye concentration at time t, k as the rate constant, and t denotes the time of the photodegradation process. The graphs of ln (C_0/C) and (C_t/C_0) versus degradation time are depicted in Figs. 3(b) and (c), respectively, with the corresponding values from Table 2 shown. The greater the k value, the greater the degradation.

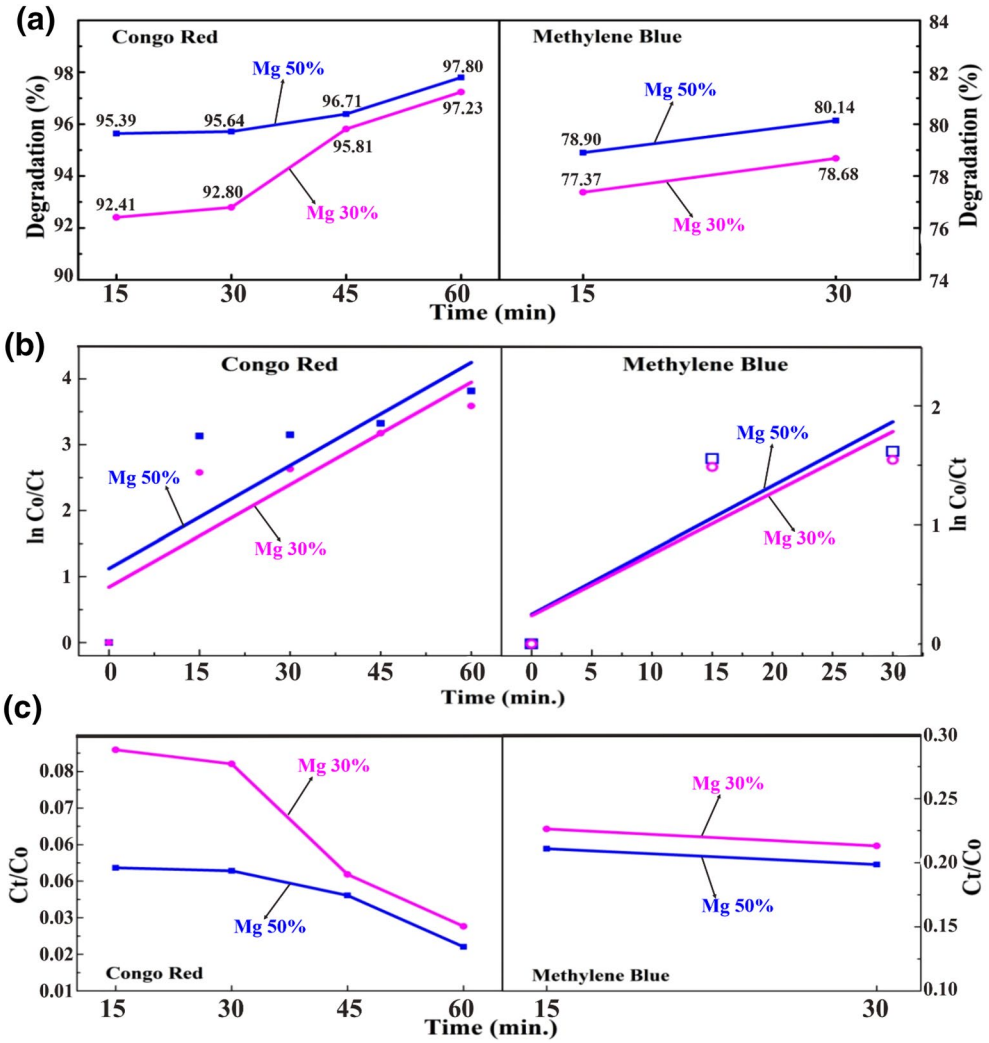

Figure 4: Degradation time vs. percentage of degradation (a) and the photocatalyst performance C_t/C_0 in ln scale (b) and a linear scale for CR and MB of composites in this study for 30% Mg and 50%.

TABLE 2: Kinetic rate constants and the percentage of degradation of CR and MB for composite in this study.

Dye	Composite	k (min^{-1})	Degradation (%)	Time (min)
CR	50% Mg	6.3×10^{-2}	97.80	60
	30% Mg	5.9×10^{-2}	97.23	60
MB	50% Mg	5.4×10^{-2}	80.14	30
	30% Mg	5.1×10^{-2}	78.68	30

The composite containing 50% Mg demonstrates the best photocatalyst performance in the degradation test using CR and MB. This confirms that Mg contributed to the suppression of electron and hole recombination [29, 34].

Photocatalyst mechanism

Due to the Schottky heterojunction of two different bandgaps, the photocatalyst mechanism for composites containing additional Mg may be possible. The Schottky heterojunction mechanism combines semiconductor and metallic materials that are useful for forming charge-free spaces between two materials. The unique s-scheme mechanism is responsible for efficiently dissociating spatial charges and maintaining high redox power [41, 44]. Light irradiates the photocatalyst material, which will excite the electron if the light energy is greater than or equal to the bandgap energy of the photocatalyst material. The high photo-carrier dissociation and photo-redox power for efficient pollutant elimination in water are associated with the spatial detachment of high-energetic carriers [45], the spatial disintegration and conservation of photo-carriers with high redox capacity, resulting in a significant improvement in photoactivity and stability [46–49]. The electron will possess the energy necessary to leap from the valence band (VB) to the conduction band (CB). The VB holes of $CoFe_2O_4$ contribute to forming hydroxide radicals (·OH). The Mg CB electrons will contribute to forming

superoxide radicals ($\cdot O_2^-$). These hydroxide and superoxide radicals contribute to the degradation of CR and MB [15] dyes. The possible reactions are as follows [38, 50]:

$$CoFe_2O_4/Mg + hCoFe_2O_4(h^+) + Mg(e^-)$$

$$H_2O + CoFe_2O_4(h^+) \rightarrow \cdot OH + H^+$$

$$O_2 + Mg(e^-) \rightarrow \cdot O_2^-$$

$$\text{Congo red/methylene blue} + \cdot OH \rightarrow \text{degradable products}$$

$$\text{Congo red/methylene blue} + \cdot O_2 \rightarrow \text{degradable products}$$

Figure 5 depicts the mechanism of the radical entering the MB and CR structures by continuously breaking bonds, with the final products being CO_2 and H_2O.

The schematic diagram of photo-redox power for efficiently removing pollutants from wastewater depicts breaking CR and MB bonds until only H_2O and CO_2 bonds are left. The formation of $\cdot O2^-$and $\cdot OH^-$radicals can be used to deduce the charge transfer mechanism from the performance degradation depicted in Fig. 4(a). Upon forming the s-scheme heterojunction with close contact, e^-would rapidly migrate from $CoFe_2O_4$ to Mg, establishing an internal electric field from $CoFe_2O_4$ to Mg and initiating band edge bending at the heterointerface [46, 47]. Metal or polymer as a co-catalyst in composite metal oxide-based materials was discovered to increase catalytic activity in the degradation reaction of organic dyes while producing hydrogen peroxide. When CR and MB bonds are broken in the medium, the catalytic activity is set to be exceptionally high.

The production of H_2O_2 from CO_2 was dependent on the chemical reaction process. The number of hydrogen ions and electrons are two crucial parameters in chemical reaction processes, but the reaction process and product are still unknown. The following chemical reactions are possible for varying amounts of hydrogen ions and electrons:

$$CO_2 + 2H^+ + 2e^-(\text{CB of } CoFe_2O_4/Mg) \rightarrow C^{2+} + H_2O_2$$

$$CO_2 + 4H^+ + 4e^-(\text{CB of } CoFe_2O_4/Mg) \rightarrow CH_2 + H_2O_2$$

$$CO_2 + 6H^+ + 6e^-(\text{CB of } CoFe_2O_4/Mg) \rightarrow CH_4 + H_2O_2$$

$$CO_2 + 8H^+ + 8e^-(\text{CB of } CoFe_2O_4/Mg) \rightarrow CH_4 + H_2 + H_2O_2$$

There are numerous pathways to produce H_2O_2 with a photocatalyst system, but future research must focus on maintaining the chemical reaction and preventing other reactions from occurring after H_2O_2 is produced.

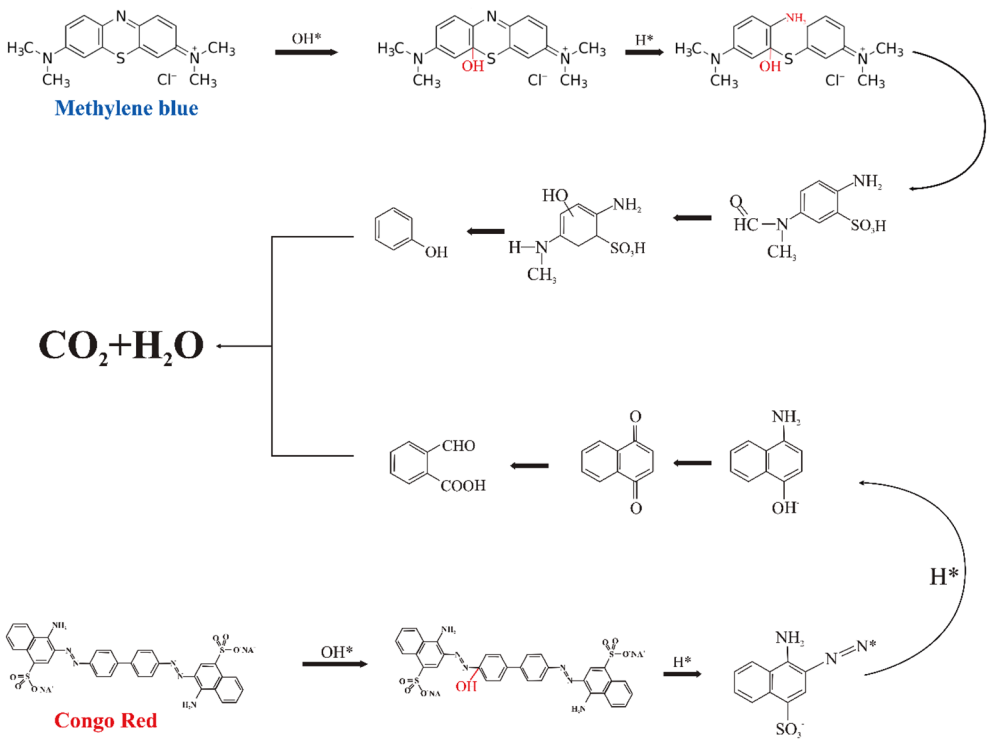

Figure 5: Schematic illustration of radical atomic bond breaking of CR and MB with the final products being H_2O and CO_2.

Reusability

Figure 6 illustrates the 50% Mg photocatalyst reused for five cycles as the basis for determining the photocatalytic efficiencies of CR and MB. After the five cycles, the degradation of CR reduced by 9.9%, while the degradation of MB reduced by up to 20.8%. According to Ref. [51], the decrease in cycle efficiency is likely due to the loss of photocatalyst mass during the washing process. Figure 7(a) depicts the XRD band diagram between Mg and $CoFe_2O_4$ and FTIR spectra of composites with 30% and 50% Mg before and after MB and CR degradation tests. The functional group derived from the FTIR spectra in Figure 7(b) is presented in Table 3. The XRD spectra in Figure 7(a) indicate that the intensity of the XRD spectra for 30% Mg decreases sharply after CR and MB are applied to the composite, whereas the XRD spectra for 50% Mg are almost identical before and after CR and MB are applied, indicating structural stability. Figure 7(b) depicts the band diagram between Mg and $CoFe_2O_4$ before degradation, which is represented by the same Fermi energy level (left), and during degradation when the electron at the VB has the energy to jump to the CB. The presence of Mg in the composite enables the electrons in the CB of $CoFe_2O_4$ to move to the CB of Mg, thereby preventing electron-hole recombination (right). The Fermi level of both Mg and $CoFe_2O_4$ increased close to the CB of $CoFe_2O_4$; this new Fermi level position acts as a trap and aids electron transport, leaving the surface state and reacting with O_2 [36, 37]. Without recombination, the hole readily escapes the VB and reacts with H_2O to produce radical atoms [36, 37]. The FTIR spectra depicted in Figure 7(c) and Table 3 reveal significant wavenumber position shifts from 0% Mg to composites with degraded CR and MB at 30% Mg but only minor shifts at 50% Mg. The chemical functional group is confirmed to be stable even after MR and CR degradation. This study demonstrates the future potential of new composite materials for textile industry wastewater treatment.

Figure 8 shows surface image of the composite ($CoFe_2O_4$)/(Mg) that indicates agglomeration between atoms of $CoFe_2O_4$ and Mg. The wide and solid surfaces will exhibit water-repellent and self-cleaning properties due to the preference for hydrophobic surfaces [52–54]. The solid surface may consist of Mg binding with Fe or Co through several oxide reactions from both metals to form FeCo–O–Mg, or it may consist of Fe–Mg or Mg–Co bonding with Fe or Co. The bonding formation affect to the electronic, electron density, and structural properties of composites [55–57].

Conclusion

According to quantitative analysis using XRD spectra, an average crystal size of 23.19 nm for CoFe2O4 containing 0% Mg, 34.28 nm for CoFe2O4 containing 30% Mg, and 27.08 nm for $CoFe_2O_4$ containing 50% Mg were obtained. Analysis of the FTIR spectrum reveals the presence of H–O–H, O–H, C–O, and M–O (M is Co and Fe) bonds, and a greater shift in wavenumbers due to an increase in Mg indicates the formation of composite $CoFe_2O_4$/Mg. The distance between the two optical phonon vibrational modes Δ(LO–TO) decreases with increasing Mg concentration, suggesting that the Mg atom has successfully attached to the surface state of $CoFe_2O_4$. The Fermi level of Mg increased close to the CB of $CoFe_2O_4$ to act as a trap and aid in electron transport, facilitating a reaction with O_2, while the

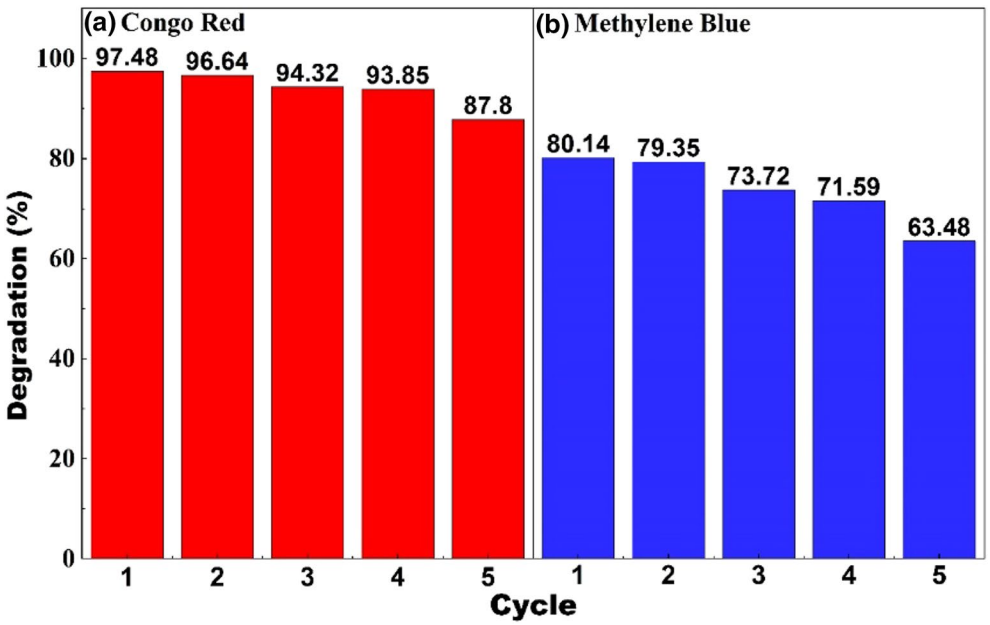

Figure 6: Cycle degradation of (a) CR and (b) MB for composite with 50% Mg in this study.

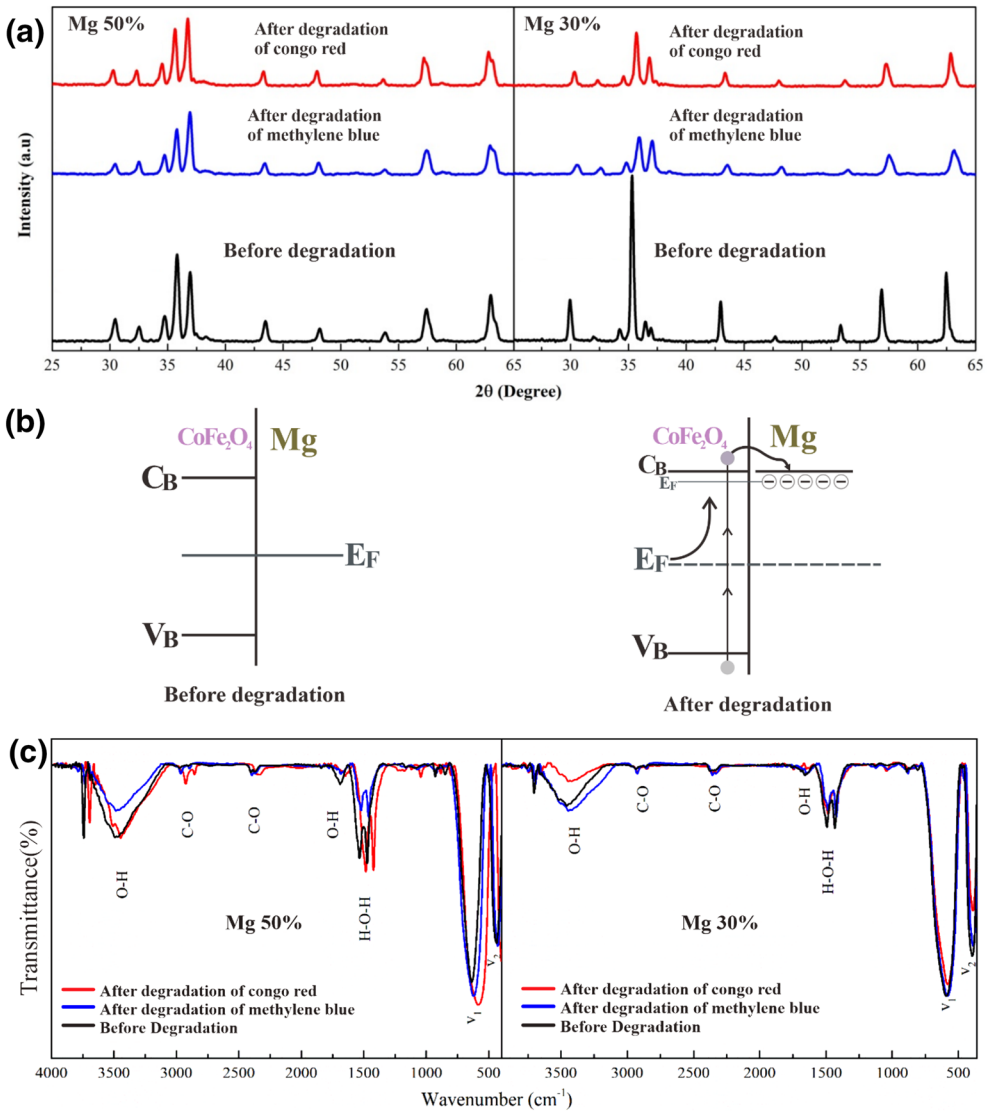

Figure 7: XRD spectra (a), schematic illustration of band diagrams between Mg and $CoFe_2O_4$ before degradation and after degradation (b), and FTIR spectra (c) for composites with 30% and 50% Mg before degradation compared with after degradation with CR and MB.

TABLE 3: The functional group derived from the FTIR spectra for comparison before degradation and after employing CR and MB to the composite for 30% Mg and 50% Mg in this study.

Composite	Functional groups (cm^{-1})						
Mg 30%	V_2	V_1	H–O–H bond	H–O bond	C–O bond	C–O bond	H–O bond
Before degradation	450	693	1471	1689	2404	2971	3490
After Congo red	404	586	1486	1651	2335	2925	3445
After Methylene blue	431	624	1462	1682	2394	2964	3485
Composite	Functional groups (cm^{-1})						
Mg 50%	V_2	V_1	H–O–H bond	H–O bond	C–O bond	C–O bond	H–O bond
Before degradation	396	592	1429	1655	2375	2934	3455
After Congo red	391	581	1435	1646	2354	2925	3419
After Methylene blue	391	581	1420	1648	2359	2925	3449

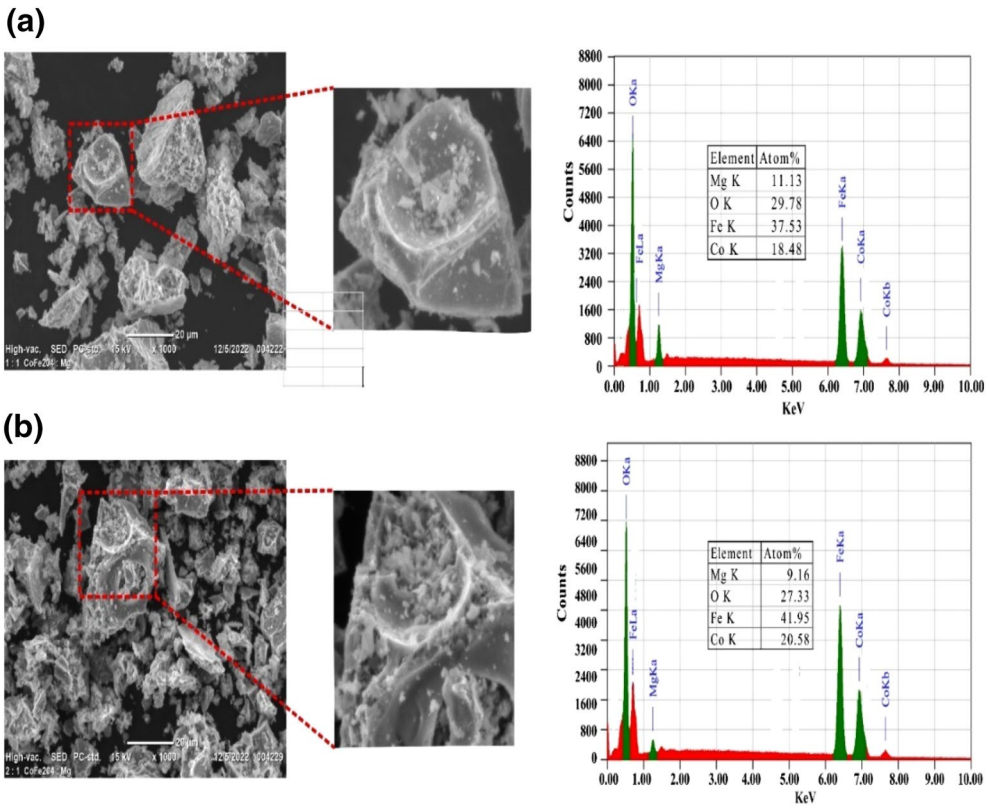

Figure 8: Surface Morphology of composite (a) SEM image of sample composite for 50% Mg and an enlarged view of the area pointed in the middle of the first line. (b) For 30% Mg, an enlarged view of the area is shown in the middle of the second line. In the last column is the EDS result that shows the atomic percentages of Mg, O, Fe, and Co element.

hole at VB moved to facilitate the reaction with H_2O to produce radical atoms. With increasing Mg, the recombination charge between the electron and hole decreases, resulting in a larger band gap. The photocatalyst degradation shows a maximum for composites with 50% Mg up to 97.80%, as well as a constant higher kinetic rate, whereas composites with 30% Mg show a maximum of 97.23%. Degradation of CR takes 60 min but only 30 min for MB. After five cycles, the reusability of the catalyst decreases by 9.9% for CR and by 20.8% for MB. The photocatalyst's efficiency demonstrates that the composite investigated in this study can potentially treat textile industry wastewater with high efficiency.

Materials and methods

Synthesis of $CoFe_2O_4$ powders

Using citric acid as an additive, cobalt ferrite powders were synthesized using the sol–gel method. In glass beakers, 20 mL of distilled water was used to dissolve 2.7 g of iron nitrate (loba chemie, 99%), 1 g of cobalt nitrate (Merck, 98%), and 2 g of citric acid. $Co(NO_3)_2{\cdot}6H_2O$: $Fe(NO_3)_3{\cdot}9H_2O$: $C_6H_8O_7$ had respective molar ratios of 1:2:3. These were stirred with a magnetic stirrer at a constant speed of 200 rpm at a temperature of 95 °C for approximately 2 h until a gel formed. $CoFe_2O_4$ powder was produced by drying the gel solution at 110 °C for 24 h and calcining it at 800 °C for 6 h in a furnace.

Preparation $CoFe_2O_4$/Mg composite

The cobalt (Co) (Merck), Iron(II) trioxide (Fe_2O_3) (supplied by Sigma Aldrich with a particle size of 50–100 nm and an assay of 97%), and magnesium powder (Mg) were obtained from Merck. The binary compound powder in the form of $CoFe_2O_4$ composite was mixed using an MM400 Retsch type mixing machine (purchased in 2011; Serial Number: 121101082213) for 1 h at a frequency of 10 Hz, followed by the simultaneous addition of Mg to the composite $CoFe_2O_4$/Mg and frequency. The mass ratio between $CoFe_2O_4$ and Mg is 70:30 with 30% Mg in the sample and 50:50 with 50% Mg in the sample for the ratio 50:50.

Photocatalyst properties test

For the evaluation of the photocatalyst, two distinct pollutants were chosen: methylene blue (MB) and Congo red (CR) as the model pollutant wastewater textile. The MB solution was made by dissolving 40 ml of MB in 1000 ml of distilled water, and

the CR solution was prepared in the same way. Each 100 ml of MB and CR solution was then transferred to a 250 ml beaker. A total of 0.3 g of sample was added to each contaminant solution, and the mixture was magnetically stirred. The photodegradation process was conducted under a 300-Watt halogen lamp and measured with a UV–vis spectrophotometer.

Reusability

$CoFe_2O_4$/Mg composite containing 50% Mg was tested for recycling because it has a faster kinetic rate. The 0.3 g was dissolved in 100 ml of CR and MB, respectively. The solution is irradiated with a halogen lamp light and stirred at a constant speed of 200 rpm. The CR solution was exposed to halogen light for 60 min, while the MB solution was exposed for 30 min. In the first cycle, the degradation solution is filtered and stored. The remaining catalyst in the solution was washed three times with distilled water and separated by centrifuging at 1500 rpm for five min and three times for five min. After that, the item was dried for 10 min at 80 °C. This process was repeated five times, after which the degradation solution was examined with a UV–vis spectrophotometer.

Material characterization

To determine the crystal structure of each sample, $CoFe_2O_4$/Mg composites were characterized using XRD ((Shimadzu 7000) with CuKα radiation ($\lambda = 1.5405$ Å $= 0.154$ nm) at a range angle of $20° \leq 2\theta \leq 70°$ operating at 30 kV and 10 mA. Using a Shimadzu IR Prestige-21 FTIR Spectrophotometer, the bonds present in the sample before and after its use as a photocatalyst were determined by FTIR analysis. Characterization of UV–vis spectroscopy using the Shimadzu UV–vis spectrophotometer UV-1800 to determine the sample's absorption spectrum.

Acknowledgments

This work was supported by the PT (Penelitian Terapan) funded by the Indonesia Government (DIKTI/BRIN) 2021 Grant: 752/UN4.22/PT.01.03/2022.

Author contributions

NF: Writing original draft. SS and HH: Software, Validation Writing original draft. DT: Writing original draft, Editing, review, and finalization.

Data availability

All data and materials generated or analyzed during this study are included in this article.

Declarations

Conflict of interest The authors declare that they have no known competing financial interests or personal relationships that could have appeared to influence the work reported in this paper.

References

1. J. Revathi, M.J. Abel, V. Archana, T. Sumithra, R. Thiruneelakandan, J. Joseph Prince, Synthesis and characterization of $CoFe_2O_4$ and Ni-doped $CoFe_2O_4$ nanoparticles by chemical Co-precipitation technique for photo-degradation of organic dyestuffs under direct sunlight. Physica B **587**, 412136 (2020)
2. L. Xu, Y. Wang, J. Liu, S. Han, Z. Pan, L. Gan, High-efficient visible-light photocatalyst based on graphene incorporated Ag_3PO_4 nanocomposite applicable for the degradation of a wide variety of dyes. J. Photochem. Photobiol. A **340**, 70 (2017)
3. A. Kalam, A.G. Al-Sehemi, M. Assiri, G. Du, T. Ahmad, I. Ahmad, M. Pannipara, Modified solvothermal synthesis of cobalt ferrite (CoFe2O4) magnetic nanoparticles photocatalysts for degradation of methylene blue with H2O2/visible light. Results Phys. **8**, 1046 (2018)
4. S. Senthilvelan, V.L. Chandraboss, B. Karthikeyan, L. Natanapatham, M. Murugavelu, TiO2, ZnO and nanobimetallic silica catalyzed photodegradation of methyl green. Mater. Sci. Semicond. Process. **16**(1), 185 (2013)
5. E. Suharyadi, A. Muzakki, A. Nofrianti, N.I. Istiqomah, T. Kato, S. Iwata, Photocatalytic activity of magnetic core-shell $CoFe_2O_4$@ZnO nanoparticles for purification of methylene blue. Mater. Res. Express **7**(8), 085013 (2020)
6. H.A.J.L. Mourão, A.R. Malagutti, C. Ribeiro, Synthesis of TiO_2-coated $CoFe_2O_4$ photocatalysts applied to the photodegradation of atrazine and rhodamine B in water. Appl. Catal. A **382**(2), 284 (2010)
7. Y. Qin, Y. Guo, Z. Liang, Y. Xue, X. Zhang, L. Yang, J. Tian, Au nanorods decorated TiO_2 nanobelts with enhanced full solar spectrum photocatalytic antibacterial activity and the sterilization file cabinet application. Chin. Chem. Lett. **32**(4), 1523 (2021)
8. M. Rahimi-Nasrabadi, M. Behpour, A. Sobhani-Nasab, M.R. Jeddy, Nanocrystalline Ce-doped copper ferrite: synthesis, characterization, and its photocatalyst application. J. Mater. Sci. **27**(11), 11691 (2016)
9. M. Li, C. Song, Y. Wu, M. Wang, Z. Pan, Y. Sun, L. Meng, S. Han, L. Xu, L. Gan, Novel Z-scheme visible-light photocatalyst based on $CoFe_2O_4$/BiOBr/graphene composites for organic dye degradation and Cr(VI) reduction. Appl. Surf. Sci. **478**, 744 (2019)
10. M. Sundararajan, L.J. Kennedy, P. Nithya, J.J. Vijaya, M. Bououdina, Visible light driven photocatalytic degradation of rhodamine B using Mg doped cobalt ferrite spinel nanoparticles

synthesized by microwave combustion method. J. Phys. Chem. Solids **108**, 61 (2017)

11. R. Zhang, L. Sun, Z. Wang, W. Hao, E. Cao, Y. Zhang, Dielectric and magnetic properties of $CoFe_2O_4$ prepared by sol-gel auto-combustion method. Mater Res Bull **98**, 133 (2018)
12. B. Abraime, K. Maalam, L. Fkhar, A. Mahmoud, F. Boschini, M.A. Tamerd, A. Benyoussef, M. Hamedoun, E.K. Hlil, M.A. Ali, A. Kenz, O. Mounkachi, Influence of synthesis methods with low annealing temperature on the structural and magnetic properties of $CoFe_2O_4$ nanopowders for permanent magnet application. J. Magn. Magn. Mater. **500**, 166416 (2020)
13. C.S. Erhardt, L.E. Caldeira, J. Venturini, S.R. Bragança, C.P. Bergmann, Sucrose as a sol-gel synthesis additive for tuning spinel inversion and improving the magnetic properties of $CoFe_2O_4$ nanoparticles. Ceram. Int. **46**(8), 12759 (2020)
14. E. Ferdosi, H. Bahiraei, D. Ghanbari, Investigation the photocatalytic activity of CoFe2O4/ZnO and CoFe2O4/ZnO/Ag nanocomposites for purification of dye pollutants. Sep. Purif. Technol. **211**, 35 (2019)
15. V. Dutta, S. Sharma, P. Raizada, A. Hosseini-Bandegharaei, V.K. Gupta, P. Singh, Review on augmentation in photocatalytic activity of $CoFe_2O_4$ via heterojunction formation for photocatalysis of organic pollutants in water. J. Saudi Chem. Soc. **23**(8), 1119 (2019)
16. M. Liu, J. Li, R. Bian, X. Wang, Y. Ji, X. Zhang, J. Tian, F. Shi, H. Cui, ZnO@Ti_3C_2 MXene interfacial Schottky junction for boosting spatial charge separation in photocatalytic degradation. J. Alloys Compd. **905**, 164025 (2022)
17. Y.-W. Liao, J. Yang, G.-H. Wang, J. Wang, K. Wang, S.-D. Yan, Hierarchical porous NiO as a noble-metal-free cocatalyst for enhanced photocatalytic H2 production of nitrogen-deficient g-C3N4. Rare Met. **41**(2), 396 (2022)
18. S. Huang, Y. Xu, M. Xie, H. Xu, M. He, J. Xia, L. Huang, H. Li, Synthesis of magnetic $CoFe_2O_4$/g-C3N4 composite and its enhancement of photocatalytic ability under visible-light. Colloids Surf. A **478**, 71 (2015)
19. S. Duangjam, K. Wetchakun, S. Phanichphant, N. Wetchakun, Hydrothermal synthesis of novel $CoFe_2O_4$/$BiVO_4$ nanocomposites with enhanced visible-light-driven photocatalytic activities. Mater. Lett. **181**, 86 (2016)
20. Y. Jia, H. Ma, C. Liu, Au nanoparticles enhanced Z-scheme Au-$CoFe_2O_4$/MoS_2 visible light photocatalyst with magnetic retrievability. Appl. Surf. Sci. **463**, 854 (2019)
21. R. Sagheer, M. Khalil, V. Abbas, Z. N. Kayani, U. Tariq, and F. Ashraf. Effect of Mg doping on structural, morphological, optical and thermal properties of ZnO nanoparticles. Optik (Stuttg) **200**, 163428 (2020).
22. S.M. Hashemi, S. Hasani, K.J. Ardakani, F. Davar, The effect of simultaneous addition of ethylene glycol and agarose on the structural and magnetic properties of $CoFe_2O_4$ nanoparticles prepared by the sol-gel auto-combustion method. J. Magn. Magn. Mater. **492**, 165714 (2019)
23. D. Carta, A. Corrias, G. Navarra, A total X-ray scattering study of MnFe2O4 nanoparticles dispersed in a silica aerogel matrix. J Non Cryst Solids **357**(14), 2600 (2011)
24. Y. Xu, S. Zhou, B. Liao, S. Zhao, X. Dai, D. Chen, Effect of milling time on the microstructure and magnetic properties of amorphous Ti50Fe50 alloys prepared by mechanical alloying. J. Market. Res. **8**(5), 3929 (2019)
25. M. Rashad, F. Pan, A. Tang, Y. Lu, M. Asif, S. Hussain, J. She, J. Gou, J. Mao, Effect of graphene nanoplatelets (GNPs) addition on strength and ductility of magnesium-titanium alloys. J. Magn. Alloys **1**(3), 242 (2013)
26. S. Rather, Synthesis, characterization, and hydrogen uptake studies of magnesium nanoparticles by solution reduction method. Mater. Res. Bull **60**, 556 (2014)
27. S.B. Vuggili, S.K. Khanth, K. Kadiya, U.K. Gaur, M. Sharma, Improvement in visible light stimulated photocatalysis by the inducement of magnesium dopant inside graphitic carbon nitride frameworks. J. Environ. Chem. Eng. **7**(6), 103440 (2019)
28. S.B. Somvanshi, M.V. Khedkar, P.B. Kharat, K.M. Jadhav, Influential diamagnetic magnesium (Mg^{2+}) ion substitution in nano-spinel zinc ferrite ($ZnFe_2O_4$): thermal, structural, spectral, optical and physisorption analysis. Ceram. Int. **46**(7), 8640 (2020)
29. M.P. Dojcinovic, Z.Z. Vasiljevic, V.P. Pavlovic, D. Barisic, D. Pajic, N.B. Tadic, M.V. Nikolic, Mixed Mg–Co spinel ferrites: structure, morphology, magnetic and photocatalytic properties. J Alloys Compd **855**, 157429 (2021)
30. H.S. Mund, B.L. Ahuja, Structural and magnetic properties of Mg doped cobalt ferrite nano particles prepared by sol-gel method. Mater Res Bull **85**, 228 (2017)
31. H. Heryanto, D. Tahir, The correlations between structural and optical properties of magnetite nanoparticles synthesised from natural iron sand. Ceram. Int. **47**(12), 16820 (2021)
32. H. Nurhasmi, A.N. Fahri, S. Ilyas, A. Ansar, B. Abdullah, D. Tahir, Study on optical phonon vibration and gamma ray shielding properties of composite geopolymer fly ash-metal. Radiat. Phys. Chem. **180**, 109250 (2021)
33. O.S. Jangong, H. Heryanto, R. Rahmat, I. Mutmainna, P.L. Gareso, D. Tahir, Effect of sugar palm fiber (SPF) to the structural and optical properties of bioplastics (SPF/Starch/Chitosan/Polypropylene) in supporting mechanical properties and degradation performance. J. Polym. Environ. **29**(6), 1694 (2021)
34. Z.T. Darmawan, H. Heryanto, I. Mutmainna, B. Abdullah, D. Tahir, Effect of magnesium (Mg) to the optical and absorption gamma-ray properties of composite shield Cassava Starch/Fe_3O_4/Mg. Radiat. Phys. Chem. **191**, 109843 (2022)
35. N. Rauf, S. Ilyas, H. Heryanto, R. Rahmat, A. N. Fahri, M. H. Rahmi, and D. Tahir: the correlation between structural and optical properties of zinc hydroxide nanoparticle in supports

photocatalytic performance. Opt. Mater. (Amst.) **112**, 110780 (2021).

36. D. Tahir, S. Ilyas, R. Rahmat, H. Heryanto, A.N. Fahri, M.H. Rahmi, B. Abdullah, C.C. Hong, H.J. Kang, Enhanced visible-light absorption of Fe_2O_3 covered by activated carbon for multifunctional purposes: tuning the structural, electronic, optical, and magnetic properties. ACS Omega **6**(42), 28334 (2021)
37. Gh.H. Khorrami, A.K. Zak, A. Kompany, R. Yousefi, Optical and structural properties of X-doped (X=Mn, Mg, and Zn) PZT nanoparticles by Kramers-Kronig and size strain plot methods. Ceram. Int. **38**(7), 5683 (2012)
38. M. Parishani, M. Nadafan, Z. Dehghani, R. Malekfar, G.H.H. Khorrami, Optical and dielectric properties of $NiFe_2O_4$ nanoparticles under different synthesized temperature. Results Phys. **7**, 3619 (2017)
39. S. Suryani, H. Heryanto, R. Rusdaeni, A.N. Fahri, D. Tahir, Quantitative analysis of diffraction and infra-red spectra of composite cement/$BaSO_4$/Fe_3O_4 for determining correlation between attenuation coefficient, structural and optical properties. Ceram. Int. **46**(11), 18601 (2020)
40. V. Elakkiya, Y. Agarwal, S. Sumathi, Photocatalytic activity of divalent ion (copper, zinc and magnesium) doped NiAl2O4. Solid State Sci **82**, 92 (2018)
41. C.A. Grande, R. Blom, V. Middelkoop, D. Matras, A. Vamvakeros, S.D.M. Jacques, A.M. Beale, M. di Michiel, K.A. Andreassen, A.M. Bouzga, Multiscale investigation of adsorption properties of novel 3D printed UTSA-16 structures. Chem. Eng. J. **402**, 126166 (2020)
42. E. Rusman, H. Heryanto, A.N. Fahri, R. Rahmat, I. Mutmainna, D. Tahir, Green synthesis ZnO/TiO2 for high recyclability rapid sunlight photodegradation wastewater. MRS Adv. **7**(21), 444 (2022)
43. X. Lu, J. Chen, M. Zheng, J. Guo, J. Qi, Y. Chen, S. Miao, B. Zheng, Effect of high-intensity ultrasound irradiation on the stability and structural features of coconut-grain milk composite systems utilizing maize kernels and starch with different amylose contents. Ultrason. Sonochem. **55**, 135 (2019)
44. S. Li, C. Wang, M. Cai, Y. Liu, K. Dong, J. Zhang, Designing oxygen vacancy mediated bismuth molybdate (Bi_2MoO_6)/N-rich carbon nitride (C3N5) S-scheme heterojunctions for boosted photocatalytic removal of tetracycline antibiotic and Cr(VI): intermediate toxicity and mechanism insight. J Colloid Interface Sci **624**, 219 (2022)
45. S. Li, M. Cai, Y. Liu, C. Wang, R. Yan, X. Chen, Constructing $Cd_{0.5}Zn_{0.5}S$/Bi_2WO_6 S-scheme heterojunction for boosted photocatalytic antibiotic oxidation and Cr(VI) reduction. Adv. Powder Mater. **2**(1), 100073 (2023)
46. M. Cai, Y. Liu, K. Dong, C. Wang, and S. Li: A novel S-scheme heterojunction of $Cd_{0.5}Zn_{0.5}S$/BiOCl with oxygen defects for antibiotic norfloxacin photodegradation: performance, mechanism, and intermediates toxicity evaluation. J. Colloid Interface Sci. **629**, 276 (2023).
47. S. Li, M. Cai, Y. Liu, C. Wang, K. Lv, X. Chen, S-Scheme photocatalyst TaON/Bi2WO6 nanofibers with oxygen vacancies for efficient abatement of antibiotics and Cr(VI): intermediate eco-toxicity analysis and mechanistic insights. Chin. J. Catal. **43**(10), 2652 (2022)
48. C. Wang, R. Yan, M. Cai, Y. Liu, S. Li, A novel organic/inorganic S-scheme heterostructure of TCPP/Bi12O17Cl2 for boosting photodegradation of tetracycline hydrochloride: kinetic, degradation mechanism, and toxic assessment. Appl. Surf. Sci. **610**, 155346 (2023)
49. M. Cai, Y. Liu, C. Wang, W. Lin, S. Li, Novel $Cd_{0.5}Zn_{0.5}S$/Bi_2MoO_6 S-scheme heterojunction for boosting the photodegradation of antibiotic enrofloxacin: degradation pathway, mechanism and toxicity assessment. Sep. Purif. Technol. **304**, 122401 (2023)
50. A. Balcha, O.P. Yadav, T. Dey, Photocatalytic degradation of methylene blue dye by zinc oxide nanoparticles obtained from precipitation and sol-gel methods. Environ. Sci. Pollut. Res. **23**(24), 25485 (2016)
51. M. Shaban, M.R. Abukhadra, A. Hamd, R.R. Amin, A.A. Khalek, Photocatalytic removal of Congo red dye using MCM-48/Ni2O3 composite synthesized based on silica gel extracted from rice husk ash; fabrication and application. J. Environ. Manag. **204**, 189 (2017)
52. X. Tan, M. Wang, Y. Tu, T. Xiao, S. Alzuabi, P. Xiang, R. Guo, X. Chen, Icephobicity studies of superhydrophobic coating on aluminium. Surf. Eng. **37**(10), 1239 (2021)
53. N.P. Shabelskaya, M.A. Egorova, E.V. Vasilieva, Synthesis and catalytic properties of $CoFe_2O_4$/Fe_2O_3 nanosized composite material. Solid State Phenom. **316**, 56 (2021)
54. Y. Li, Y. Bi, M. Zhang, S. Zhang, X. Gao, Z. Zhang, Y. He, Hollow cathodic plasma source nitriding of AISI 4140 steel. Surf. Eng. **37**(3), 351 (2021)
55. A. Ardiansyah, R. Rahmat, M. Azlan, H. Heryanto, and D. Tahir: Nanocrystal composites cement/$BaCO_3$/Fe_2O_3 for improved X-ray shielding characteristics: stability structural properties. J Mater Res (2022).
56. Muh. S. Gharissah, A. Ardiansyah, S. R. Pauziah, N. A. Muhammad, R. Rahmat, H. Heryanto, and D. Tahir: Composites cement/$BaSO_4$/Fe_3O_4/CuO for improving X-ray absorption characteristics and structural properties. Sci. Rep. **12**(1) (2022).
57. H. Heryanto, D. Tahir, High absorption electromagnetic wave properties of composite $CoFeO_3$ synthesized by simple mechanical alloying. CS J. Solid State Sci. Technol. **10**(12), 123015 (2021)